Journal of Geophysical Research: Atmospheres

RESEARCH ARTICLE
10.1029/2018JD028281

The Study of Inland Eyewall Reformation of Typhoon Fanapi (2010) Using Numerical Experiments and Vorticity Budget Analysis

Ming-Jen Yang[1], **Yao-Chu Wu**[1], **and Yu-Chieng Liou**[2]

[1]Department of Atmospheric Sciences, National Taiwan University, Taipei, Taiwan, [2]Department of Atmospheric Sciences, National Central University, Chung-Li, Taiwan

Key Points:
- The Fanapi eyewall breaks down over the Taiwan terrain and reforms again
- Terrain and surface friction over land weaken the updraft and reduce the width and depth of vortical hot towers
- Vortical hot towers in land cooperate with rainband through horizontal vorticity advection to rebuild Fanapi eyewall

Correspondence to:
M.-J. Yang,
mingjen@as.ntu.edu.tw

Citation:
Yang, M.-J., Wu, Y.-C., & Liou, Y.-C. (2018). The study of inland eyewall reformation of Typhoon Fanapi (2010) using numerical experiments and vorticity budget analysis. *Journal of Geophysical Research: Atmospheres*, *123*. https://doi.org/10.1029/2018JD028281

Received 4 JAN 2018
Accepted 13 AUG 2018
Accepted article online 24 AUG 2018

Author Contributions:
Conceptualization: Ming-Jen Yang
Formal analysis: Ming-Jen Yang
Investigation: Ming-Jen Yang, Yao-Chu Wu, Yu-Chieng Liou
Methodology: Ming-Jen Yang
Resources: Yao-Chu Wu, Yu-Chieng Liou
Validation: Yu-Chieng Liou
Writing - original draft: Ming-Jen Yang
Writing – review & editing: Yu-Chieng Liou

Abstract Numerical simulations of Typhoon Fanapi (2010) interacting with the terrain of Taiwan are conducted using the Advanced Research Weather Research and Forecasting model (ARW, version 3.3.1) on a triply nested grid (with the finest grid size of 1 km and 55 vertical levels). Fanapi made landfall on eastern Taiwan at 0000 UTC 19 September and left Taiwan at 1200 UTC 19 September 2010, producing heavy rainfall and severe floods. After landfall, the Fanapi eyewall weakened and broke down over the Central Mountain Range. Vortical hot towers (VHTs) occurred along the Fanapi rainband, and the VHTs in land have weaker maximum updrafts (7.0–8.0 m/s), narrower diameter (7.0–11.5 km), and shallower depth (6.5–9.0 km), compared with oceanic VHTs over the Taiwan Strait. The VHTs over the Taiwan Strait remained organized along the rainband and propagated toward the southeast quadrant of the Fanapi circulation over land by the tangential flow. These organized VHTs in the southeast quadrant help transport cyclonic vorticity from lower into middle levels and then cooperate with the rich vorticity within the rainband by horizontal vorticity advection to rebuild the Fanapi eyewall upward from the bottom. The vorticity balance within the entire Fanapi circulation is largely dominated by its southeast quadrant with organized VHTs over Taiwan Island. In the simulation with no latent heat release, the VHTs quickly decay and radiate outward from the eyewall as gravity-wave perturbations.

Plain Language Summary In this manuscript, we have examined the eyewall reconstruction process of Typhoon Fanapi (2010) over Taiwan Island using numerical experiments and vorticity budget calculations based on the high-resolution model outputs. Our findings explain how the eyewall originally broken down by the Taiwan terrain could be reconstructed through the interactions between vortical hot towers and primary rainband. We believe that these findings would be scientifically interesting and useful to weather forecasters and general readers.

1. Introduction

The steep terrain over the Central Mountain Range (CMR) of Taiwan can substantially alter the track of a tropical cyclone (TC) that crosses the island. Chang (1982) in his idealized simulation showed that the original low-level TC center was blocked by the CMR, and a secondary low-level circulation center formed in the lee side. Yeh and Elsberry (1993a, 1993b), Lin et al. (2005), and Lee et al. (2008) utilized numerical simulations to examine the rainfall distribution and track deflection induced by orographic effects when a TC passed over a mountainous island like Taiwan. Jian and Wu (2008) and Huang et al. (2011) found that the terrain height of Taiwan played an important role in determining the looping motion of TC, through a series of terrain-height sensitivity experiments. Wu and Kuo (1999), Wu et al. (2002), and Yang et al. (2008) showed that TC's storm structure, intensity, and rainfall distributions can be altered significantly by the CMR.

When TCs make landfall on a mountainous island, TC eyewall structure can change substantially due to the interaction between the TC circulation and the terrain. Wu et al. (2003) and Wu et al. (2009) used satellite data and a numerical simulation to illustrate that when TC Zeb (1998) made landfall at Luzon Island, the eyewall experienced contraction before landfall, weakening and breakdown during landfall, and reformation after moving offshore. By statistically examining the characteristics of 23 TCs crossing the Philippines and 6 TCs crossing Taiwan, Chou et al. (2011) found that the radius of the eyewall increased during landfall for 87% of the TCs, while 57% of these TCs with expanded eyewalls experienced eyewall contraction.

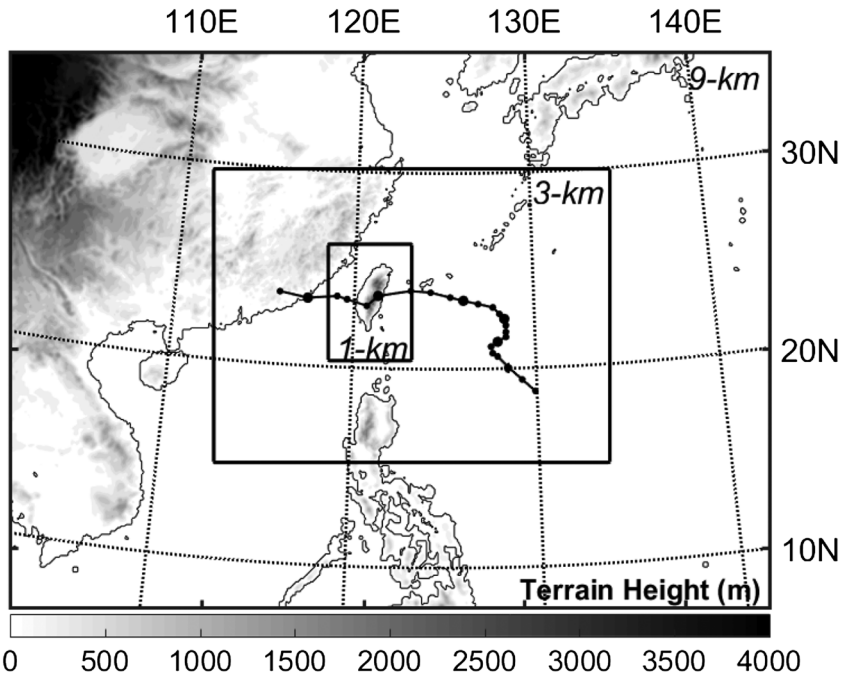

Figure 1. Three nested domains (with the horizontal grid size of 9, 3, and 1 km, respectively) of the Weather Research and Forecasting model used in this study. The 6-hourly best track of Fanapi from the Joint Typhoon Warning Center, starting from 1200 UTC 14 September and ending at 0600 UTC 20 September 2010 (the large dots denote the position at 0000 UTC), is indicated. Terrain height on the 9-km grid is shaded.

Vortical hot towers (VHTs) are characterized by deep convection with collocated updrafts and cyclonic vertical vorticity. These tall convective towers with cyclonic rotation can develop upward and possibly reach the tropopause. Numerical studies (Hendricks et al., 2004; Montgomery et al., 2006) indicate that VHTs play an important role in an upscale transport process in which convective-scale vorticity anomalies can act collectively to convert a tropical disturbance into a TC. These VHTs transport cyclonic vorticity upward, moisten the troposphere, and can merge with nearby convective towers. Several studies (Houze Jr. et al., 2009; Reasor et al., 2005; Sippel et al., 2006) provide observational documentation of the role of VHTs in the formation of TCs. Reasor et al. (2005) observed from the aircraft and radar data that multiple low-level and midlevel mesoscale vortices were collocated with deep convection within the pre-TC disturbance prior to the genesis of Hurricane Dolly (1996). Using the airborne Doppler radar data, Houze Jr. et al. (2009) documented that for the tropical depression leading to the genesis of Hurricane Ophelia (2005), the VHTs were typically 10-km wide and 17-km deep with updrafts of 10–20 m/s throughout the middle to upper troposphere. The interplay between the vorticity perturbations at lower and middle levels in VHTs and the surrounding stratiform regions was hypothesized to be responsible for the upscale transfer of vorticity from the convective scale and stratiform regions to trigger the genesis of Hurricane Ophelia.

Liou et al. (2016, hereafter LWH) documented observational changes in the eyewall of Typhoon Fanapi (2010) after the landfall on Taiwan. Fanapi's eye and eyewall first disappeared on the eastern side of Taiwan's CMR after landfall but reappeared on its western side. All observational data including the cyclonic circulation, the distribution of updrafts and downdrafts, and surface low pressure and intense rainfall indicated a reconstructed eyewall. The signatures of VHTs within the reintensified eyewall were also shown in their radar data analysis.

Nevertheless, the underlying mechanism of Fanapi's eyewall reformation over Taiwan terrain has not been investigated in detail. Thus, a fundamental scientific question to ask in this study is how Typhoon Fanapi (2010) reformed its eyewall structure after crossing the Taiwan terrain? There are two possible scenarios, including (1) the top-down process whereby the downward transport of midlevel TC vortex into lower levels over the lee (western) side of the CMR occurs, while the original low-level TC center is still blocked by the CMR, and (2) the bottom-up process, which involves the upward transport and reconnection of a low-level vorticity center with its midlevel counterpart, resulting in a complete reformation of a TC eyewall. In this

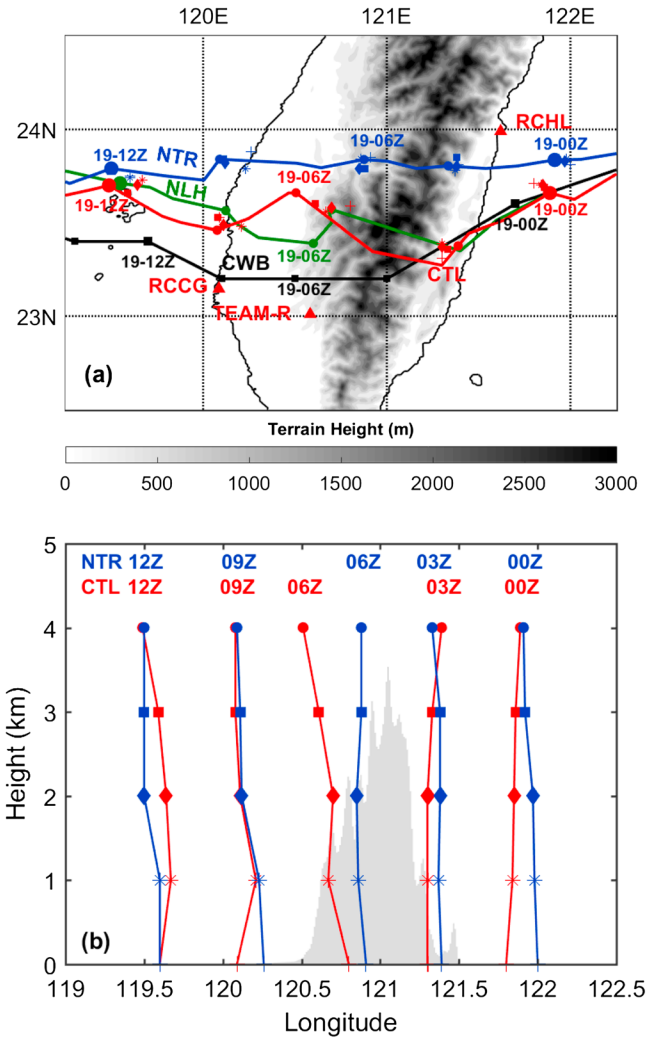

Figure 2. (a) The three-hourly tracks of Typhoon Fanapi from the Central Weather Bureau (CWB) best track (black line), and the hourly tracks of control (CTL; red line), no-terrain (NTR; blue line), and no-latent-heating (NLH; green line) experiments, and (b) the vertical cross section showing the simulated Fanapi centers at different heights for the CTL (in red) and NTR (in blue) experiments every 3 hr along the 23.5°N latitude from 0000 UTC 19 September to 1200 UTC 19 September 2010. The large dots denote tropical cyclone center positions at 0000 and 1200 UTC. Circulation center at 4-, 3-, 2-, and 1-km level of CTL and NTR experiments is indicated by circle, square, diamond, and asterisk, respectively. Sea level pressure center of CTL and NTR experiments is indicated by plus sign. Note that the lines in (a) connect the 4-km storm centers, not the sea level pressure centers. Locations of operational radar of Hualien (RCHL), Chigu (RCCG), and TEAM-R mobile radar are indicated. Terrain height on the 1-km grid is shaded in (a) and is in gray color in (b).

study, numerical experiments and vorticity-budget calculations are conducted to investigate possible mechanisms for Fanapi's eyewall reformation.

Model description and sensitivity experiments are introduced in section 2. Model verification is in section 3, vorticity budget analysis is in section 4, and results of sensitivity experiments are discussed in section 5. Finally, conclusions are given in section 6.

2. Model Description

In this study, the Advanced Research Weather Research and Forecasting model (ARW version 3.3.1; Skamarock et al., 2008) is used to simulate TC Fanapi (2010) from 1800 UTC 17 September to 0600 UTC 20 September 2010, with a forecast period of 60 hr. The triply nested domains (Figure 1) have horizontal grid sizes of 9, 3, and 1 km, respectively, and the nests do not move with the storm center. Two-way interaction between inner and outer grids is considered. Fifty-five eta (η) levels are used in the vertical direction with higher resolution within the planetary boundary layer (finest vertical grid size is 40 m near the surface) and near the tropopause. The model top is at 30 hPa.

The physical parameterization schemes used in the model include the Grell-Devenyi ensemble cumulus parameterization (Grell & Dévényi, 2002), the double-moment Morrison microphysics parameterization (Morrisson et al., 2005; Morrisson & Gettelman, 2008), Rapid Radiative Transfer Model (RRTM) longwave radiation parameterization (Mlawer et al., 1997), Dudhia (1989) shortwave parameterization, and the Yonsei University (YSU) planetary boundary layer parameterization (Hong & Pan, 1996). Note that cumulus scheme is used in the outermost (9-km) gird only, assuming that the grid sizes of the intermediate (3-km) and innermost (1-km) grids are fine enough to explicitly resolve convection. The initial and boundary conditions are from the European Centre for Medium Range Weather Forecasts/Tropical Ocean Global Atmosphere (ECMWF/TOGA) analysis data set, which are updated every 6 hr with the latitude-longitude resolution of 1.125°. To maintain the numerical stability for deep-convection simulation above complex topography, a sixth-order numerical diffusion (Knievel et al., 2007; Xue, 2000) with a damping factor of 0.08 and the vertical-velocity damping are used. The sea surface temperature remains constant throughout model simulation. In addition to the full-terrain control simulation (CTL), a no-terrain (NTR) experiment with the same model setting as the CTL, except that the Taiwan terrain is completely removed, is performed to examine the impacts of Taiwan terrain on the track and eyewall reformation process of TC Fanapi. To examine the effects of latent heating and cooling on the maintenance of the TC vortex and VHTs, the no-latent-heating (NLH) experiment is also conducted, where the latent heating and cooling was turned off 3 hr before the CTL-simulated Fanapi made landfall on Taiwan (i.e., after 0000 UTC 19 September because the CTL storm made landfall at 0300 UTC).

3. Model Verification

3.1. Typhoon Track and Intensity

Typhoon Fanapi (2010) was formed over the Western North Pacific Ocean as a tropical depression at 1200 UTC 14 September 2010 and moved northwestward slowly (see Figure 1). At 0000 UTC 15 September, the Joint Typhoon Warning Center (JTWC) categorized Fanapi as a tropical storm. Based on the JTWC data,

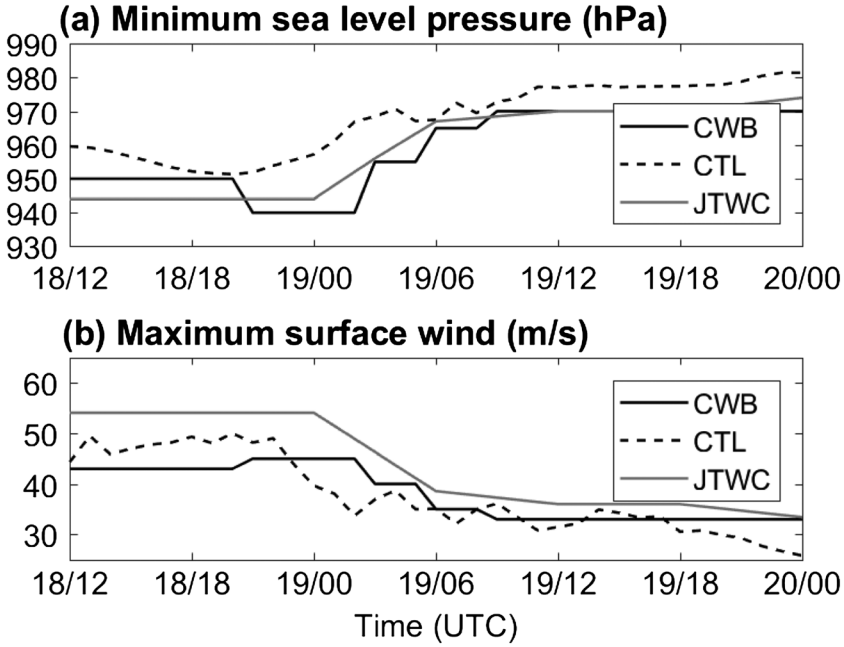

Figure 3. The time series of storm intensity of Fanapi: (a) central minimum sea level pressure (in units of hPa) and (b) near-surface (10 m above ground level) maximum wind (in units of m/s). The solid line is for the Central Weather Bureau (CWB) best-track analysis, the dashed line is for the control (CTL) simulation, and the gray line is for Joint Typhoon Warning Center (JTWC) best-track analysis.

Fanapi reached to the TC intensity (category 1) at 1200UTC 16 September. According to the Central Weather Bureau (CWB) in Taiwan, Fanapi made landfall over Hualien County on the east coast of Taiwan at 0040 UTC 19 September (Figure 2a). While approaching the Taiwan terrain, Fanapi started to deflect southward (see the CWB best track in Figure 2a).

Figure 2a shows the comparison between the CWB best track (in black) and the simulated tracks (red for the CTL, blue for the NTR, and green for the NLH) during the landfall period from 0000 UTC to 1200 UTC 19 September 2010. The southward track deflection of the observed storm by the CMR is captured by the CTL simulation, although the departure position of the CTL is ~30 km north to its observed counterpart. There is some timing error in the CTL simulation; to be specific, the CTL storm made landfall on eastern Taiwan over the observed location 2.5 hr later than the observed storm, but left Taiwan 1 hr earlier. When the observed Fanapi moved toward the eastern side of CMR, its translation speed decreased. The storm in the NTR experiment made landfall over Hualien 1 hr earlier than in the CTL experiment. The earlier landfall time for the NTR experiment may result from the decreased topographic blocking effect and reduced surface friction (similar earlier landfall time for the NTR run was also indicated for Typhoon Nari [2001] by Yang et al., 2008).

The southward track deflection of Fanapi is associated with terrain blocking and channeling effect (Jian & Wu, 2008; Lin et al., 2002; Wu et al., 2012). When a TC vortex approaches the Taiwan Island, the air mass accumulates and builds up a local high pressure on the windward side. The pressure gradient between the TC vortex center and the CMR increases such that low-level northerly flow is reinforced. The strong northerly jet then results in a southward deflection of TC track. This southward track deflection of TC Fanapi is consistent with other idealized (Lin et al., 1999) and real-case TC modeling studies over the same region (Jian & Wu, 2008; Yang et al., 2008). Both Yang et al. (2008) and Huang et al. (2016) found that the translation speed of typhoons decreased before their landfall on Taiwan.

In addition to track deviation, the steep terrain on CMR also imposes a significant tilting of TC circulation center in the vertical (Figure 2b). For the CTL run, the TC circulation centers remained relatively coherent in the vertical at 0000 and 0300 UTC; the TC circulation center at 4-km level is to the west of the 2-km center at 0600 UTC, due to the CMR blocking; at 0900 UTC when the Fanapi center is near the coast, the TC circulation centers remain vertically aligned again (red lines in Figure 2b). In contrast, in the absence of CMR terrain, the TC circulation centers have less vertical TIL in the NTR experiment (blue lines in Figure 2b).

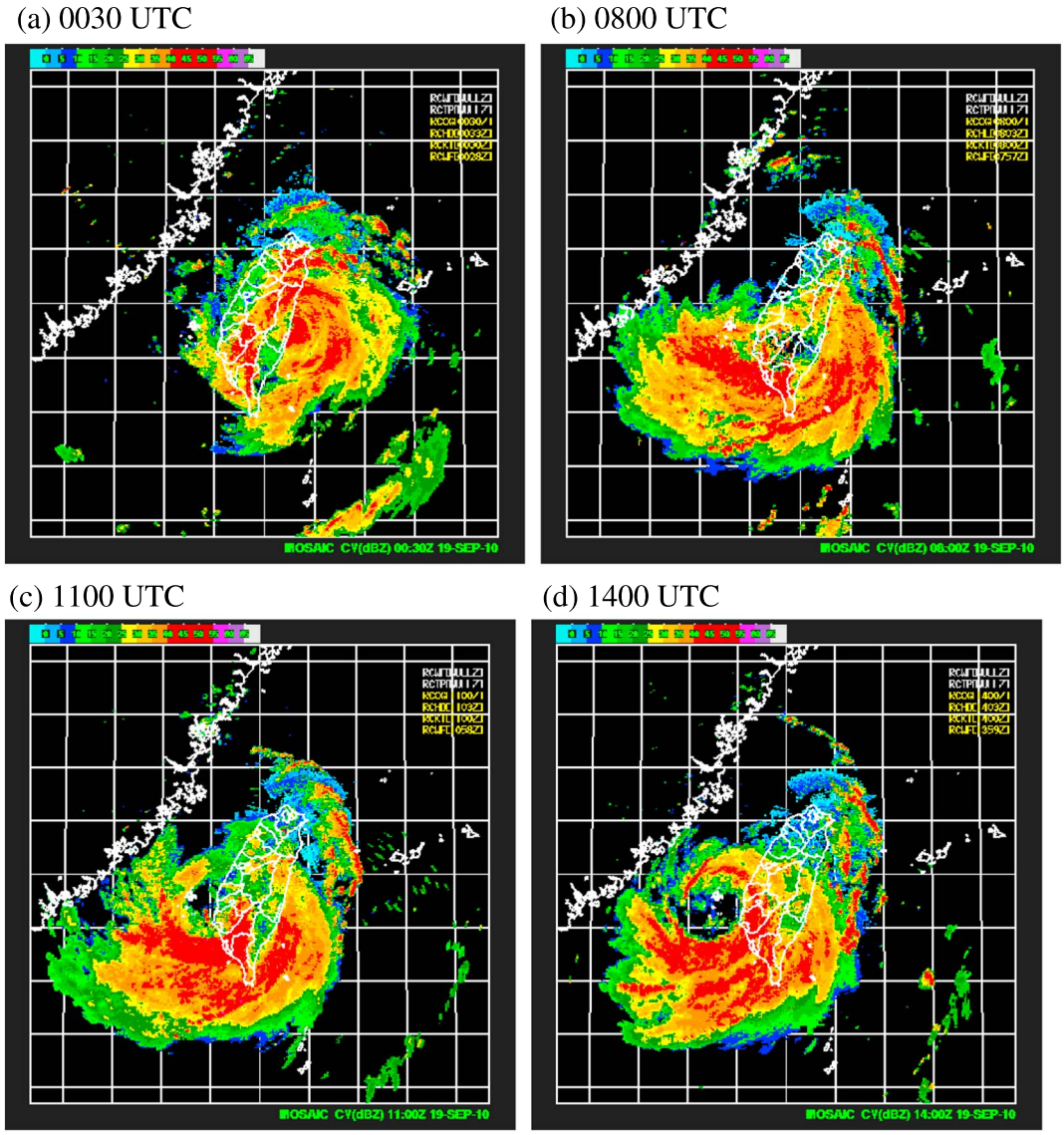

Figure 4. Radar reflectivity composite of Typhoon Fanapi at (a) 0030, (b) 0800, (c) 1100, and (d) 1400 UTC 19 September 2010 from the Central Weather Bureau.

Figure 3 illustrates the time series of central minimum sea level pressure and near-surface (10 m above ground level) wind maximum of the observed storm (from CWB and JTWC best-track analyses) and the CTL run from 1200 UTC 18 September to 0000 UTC 20 September 2010. Note that the maximum sustained wind from the JTWC best- track analysis is for 1-min mean but that for the CWB best-track analysis is for 10-min mean; this is the reason why the JTWC analysis shows a stronger storm than the CWB analysis for the maximum surface wind (Figure 3b). According to CWB best-track analysis, Fanapi had the strongest storm intensity with a central sea level pressure of 940 hPa and a maximum wind speed of 45 m/s just before making landfall on Taiwan Island at 00 UTC 19 September. When Fanapi was over the island (00–12 UTC 19 September), the central minimum pressure filled to 970 hPa and the maximum near-surface wind decreased to 33 m/s. The CTL simulation showed similar intensity evolution (decreased storm intensity) during the landfall period; the CTL storm had a slightly weaker intensity than the observed during and after landfall.

3.2. Radar Reflectivity and Wind Structure

While passing the CMR, Fanapi's primary rainband encountered the steep terrain and produced torrential rainfall over central and southwestern Taiwan (Figures 4a and 4b). The eyewall of Fanapi was first broken

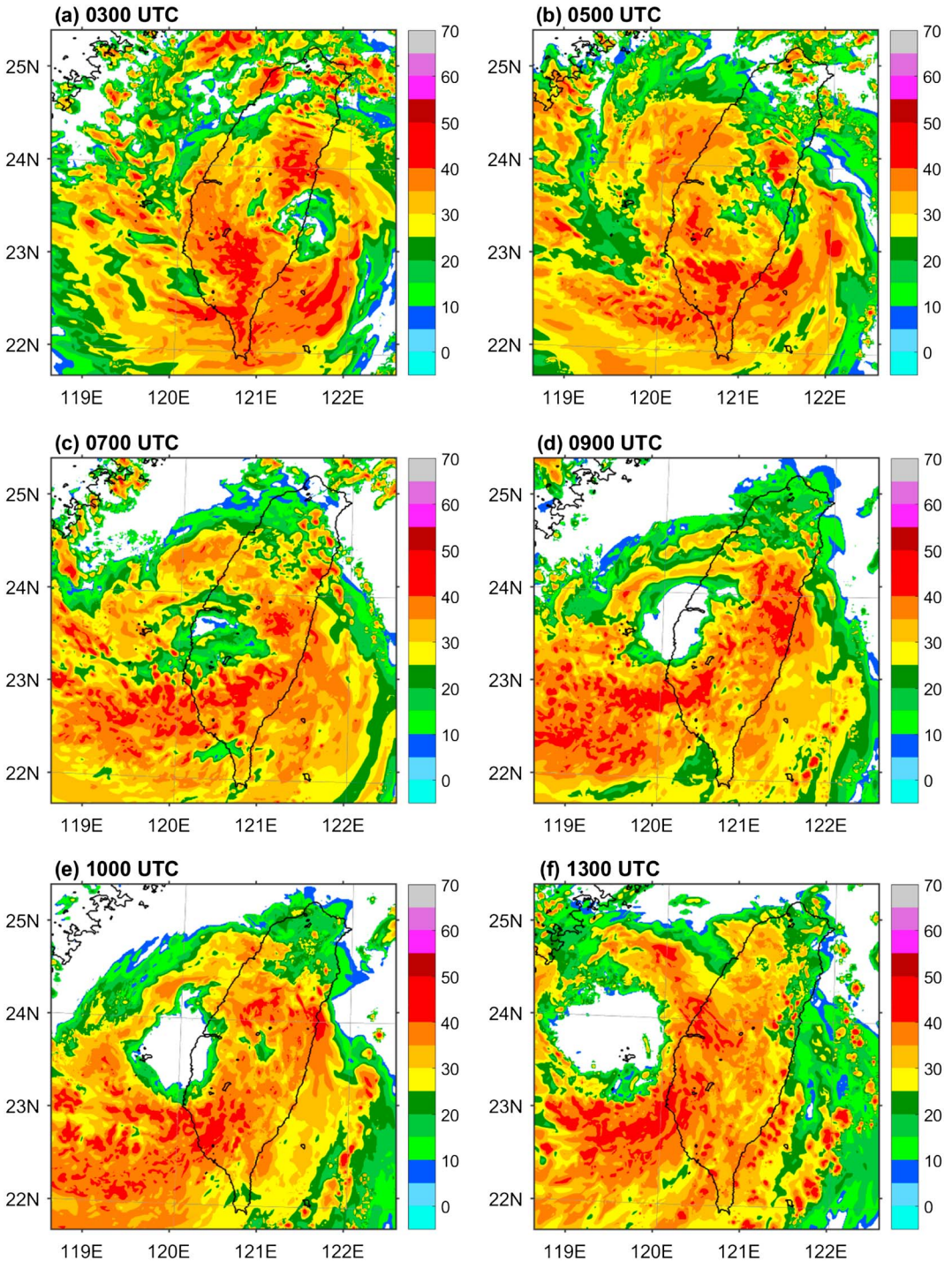

Figure 5. Composite of simulated maximum radar reflectivity (in units of dBZ) at (a) 0300, (b) 0500, (c) 0700, (d) 0900, (e) 1000, and (f) 1300 UTC 9 September 2010 from the control experiment.

down by the CMR complex topography but reorganized in the western side of the CMR by 1100 UTC 19 September (Figure 4c). While moving offshore from Taiwan to Penghu Island, Fanapi produced heavy rainfall over southern and central Taiwan with the reconstructed eyewall (Figure 4d). The simulated radar reflectivity from the CTL experiment is in Figure 5, which is in good agreement with the CWB radar composite (Figure 4) and the hourly reflectivity analysis (see Figure 6 of the LWH). Note that the time difference between the

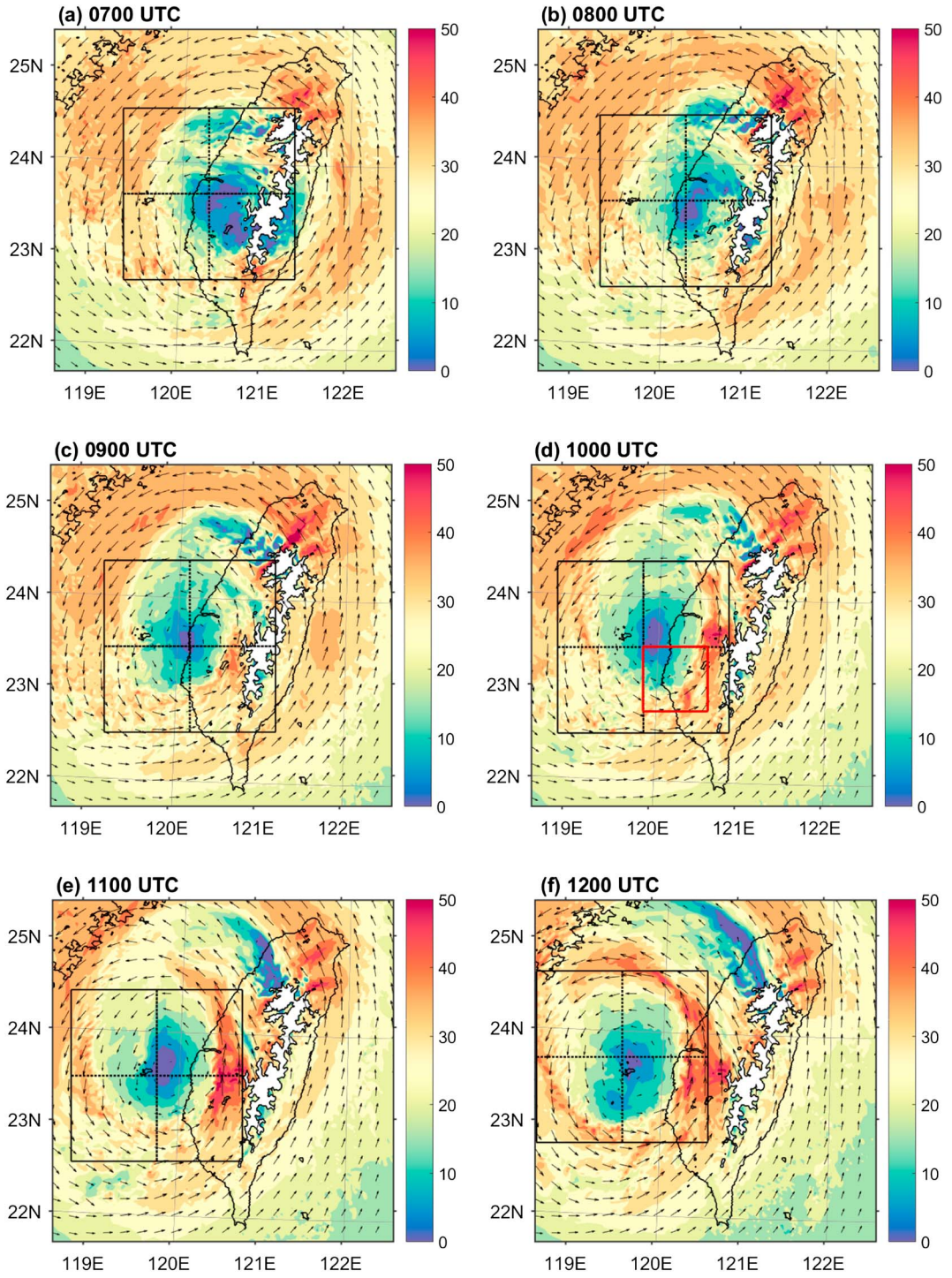

Figure 6. Simulated horizontal wind vector and speed (colored; in units of m/s) from the CTL at (a) 0700, (b) 0800, (c) 0900, (d) 1000, (e) 1100, and (f) 1200 UTC 19 September at 2-km height. The red box in Figure 6d is for the square of 75 km by 75 km in Figure 8. A box with four squares (each of the size of 100 km by 100 km) centered on the tropical cyclone eye is plotted.

observed (Figure 4) and simulated (Figure 5) radar composites is due to timing error of the simulated Fanapi versus the observed.

Figures 4 and 5 are the observed and simulated radar reflectivity composites over Taiwan during the landfall period of Typhoon Fanapi, respectively. At the time of landfall (Figures 4a and 5a), the TC eye became difficult

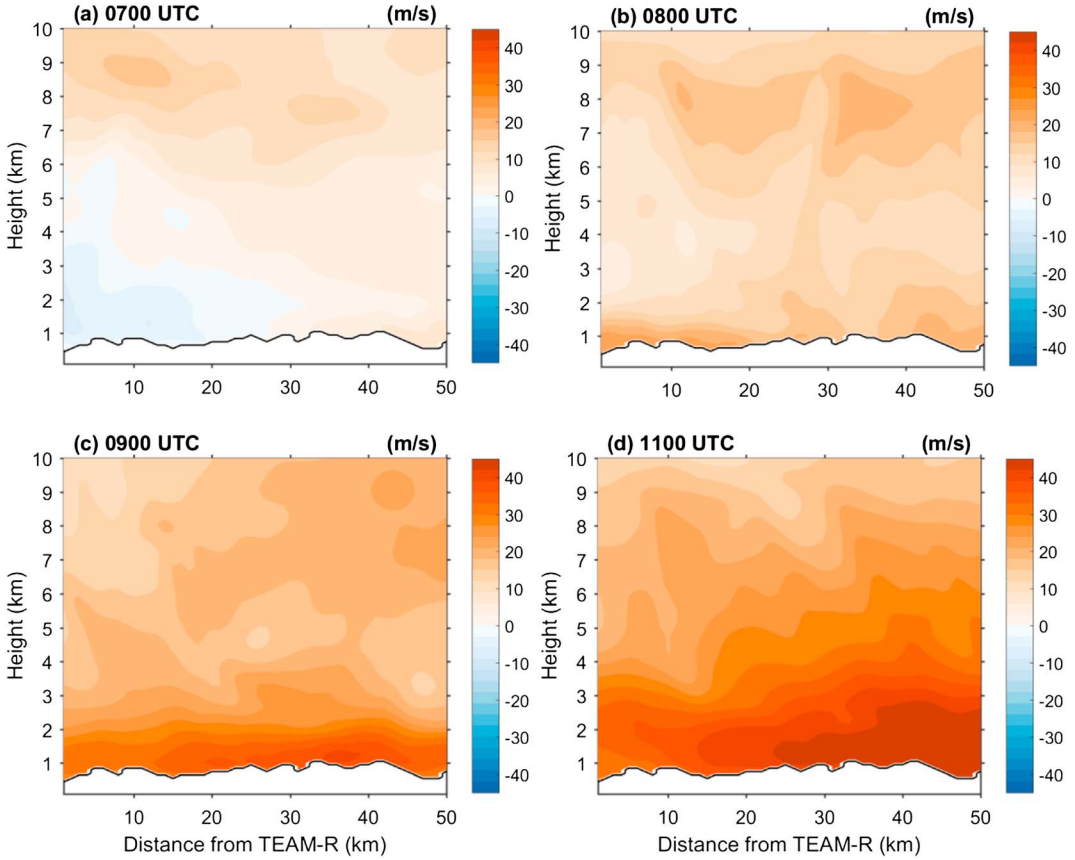

Figure 7. Vertical cross section of meridional wind (red for southerly and blue for northerly; in units of m/s) diagnosed from the control simulation at (a) 0700, (b) 0800, (c) 0900, and (d) 1100 UTC 19 September at the TEAM-R radar location along the north-south direction. The location of TEAM-R radar is shown in Figure 2.

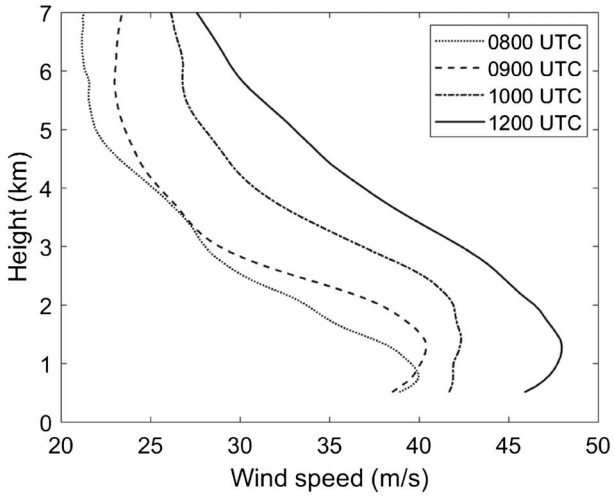

Figure 8. The vertical profile of the horizontal wind speed averaged over a horizontal square of 75 km by 75 km to the SE of Fanapi center at 0800, 0900, 1000, and 1200 UTC. The horizontal position of the square is indicated by the red box in Figure 6d.

to identify because precipitation formed near the center due to the effects of the steep CMR terrain and enhanced surface friction. When Fanapi center moved to the western plain of CMR (Figures 4b and 5b), the primary rainband occurred in east-west orientation and was almost perpendicular to the CMR. The intense convective cells within the primary rainband, developed in the Taiwan Strait, moved eastward and caused torrential rainfall record near Kaohsiung (see Figure 7 of LWH for the intense rainfall at Guansan station). Later, the primary rainband had more cyclonic curvature and moved further to the north (Figures 4c and 5c and 5d). Fanapi's eyewall appeared more asymmetric after crossing the CMR during 06–12 UTC when the eyewall reformed as Fanapi was emerging from the west coast of Taiwan. The northern part of Fanapi eyewall had weaker radar reflectivity than the southern part. The weaker radar echo in the northern part might be associated with the raindrop evaporation and graupel sublimation on the lee (western) side of the CMR as the TC tangential flow passed over the CMR and subsided on the lee side. Other factors such as surface flux asymmetry and vertical wind shear may also contribute to the precipitation asymmetry. When Fanapi vortex moved over the Taiwan Strait (Figures 4d and 5e and 5f), the primary rainband developed into a circular-shape eyewall and the eyewall reorganized eventually.

Figure 6 displays the simulated horizontal wind field at 2 km during the time period of 0700–1200 UTC, and a box with four squares (each of the

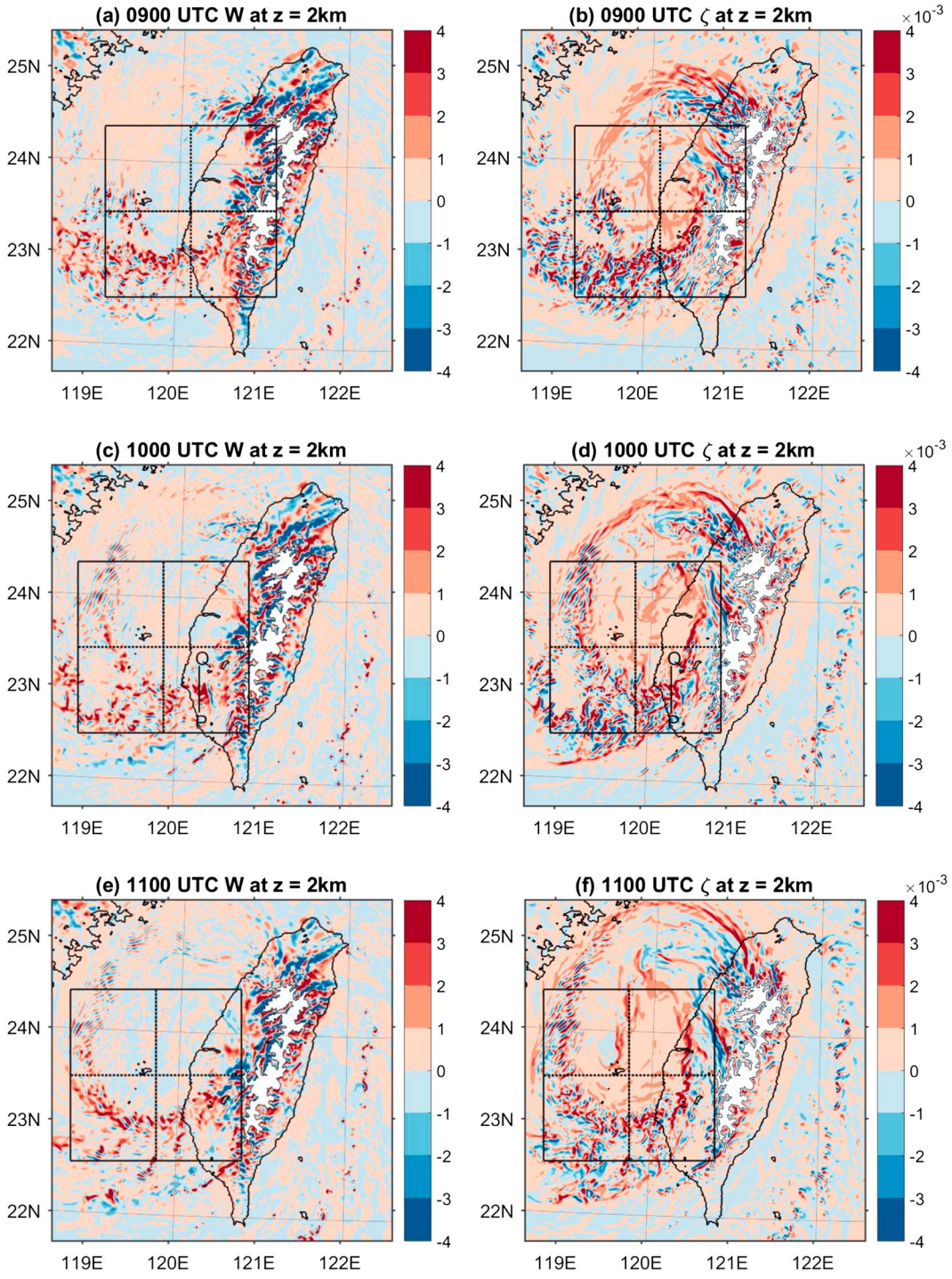

Figure 9. Simulated vertical velocity and vertical vorticity at (a and b) 0900, (c and d) 1000, and (e and f) 1100 UTC 19 September 2010 at $z = 2$ km. The figures in (a), (c), and (e) are for the vertical velocity (in m/s), and the figures in (b), (d), and (f) are for vertical vorticity (in 10^{-3}/s). A box with four squares (each of the size of 100 km by 100 km) centered on the tropical cyclone eye is plotted. PQ is for the horizontal position of the vertical cross section in Figure 11.

size of 100 km by 100 km) centered on the TC eye is plotted on each panel. When the TC moved across the island, the eyewall gradually broke down and the wind near the TC eye was generally less than 10 m/s (Figures 6a and 6b), but strong downslope wind of more than 40 m/s occurred over northern Taiwan

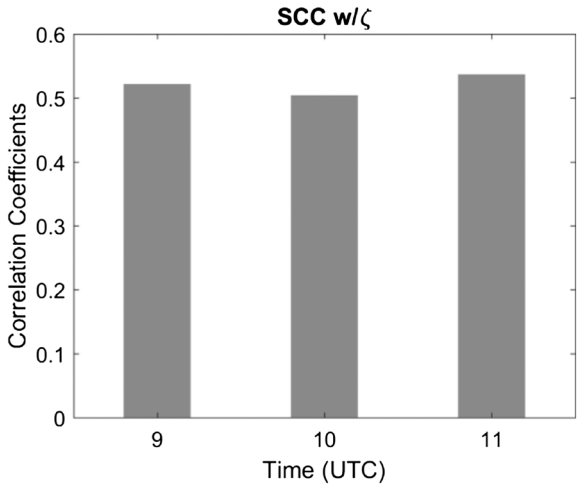

Figure 10. Spatial correlation coefficient (SCC) between vertical velocity and vertical vorticity within the vortical hot towers at 0900, 1000, and 1100 UTC 19 September 2010.

(Figure 6b). At 1000 UTC, the TC eye moved slightly offshore of western Taiwan and reached southerly winds over 30 m/s (Figure 6d). In the following hours (1100 and 1200 UTC; Figures 6e and 6f), the area associated with strong wind of greater than 30 m/s (next to the western edge of the CMR) expanded and had a cyclonic curvature, in agreement with the reconnected eyewall shown in radar reflectivity field (Figures 5e and 5f). Note that the analysis times are not the same between Figures 5 and 6. Also, note that LWH used multiple Doppler radars (RCCG, RCMK, RCKT, and TEAM-R; see the radar locations in Figure 2) to retrieve low-level horizontal wind flows of Fanapi, and our simulated wind field over the southwestern Taiwan is in general agreement with their retrieved wind field (see their Figure 8).

The TEAM-R radar was located at 23.01°N, 120.583°E (see Figure 2 for its location) and was doing a Range-Height-Indicator (RHI) scan pointing to the north during 0800–1200 UTC. Figure 7 shows the simulated meridional wind from the TEAM-R location in the CTL simulation along the north-south direction, which can be compared with Figures 11e–11h in LWH. In Figures 7a–7d, the southerly jet was strengthened from low level to middle level. The radar-observed southerly wind reached 35 m/s, and the depth of strong southerly flow was increased from 2 to 6.5 km in 3 hr (Figures 11e–11h in LWH). The CTL simulation indicates that the southerly wind attained to 40 m/s and the depth of southerly flow of over 25 m/s reached 5 km in Figure 7d. The acceleration and upward depth expansion of southerly flow with time could be an important indication of the bottom-up process.

Figure 8 shows the vertical profile of the horizontal wind speed averaged over a square of 75 km by 75 km over the southwest plain of the CMR during the time period of 0800–1200 UTC when Fanapi was located in the western plain of CMR and about to leave Taiwan Island. For comparison purpose, this square is located at approximately the same region used for Figure 12 of LWH, although the timing and track errors of the simulated TC add complication to the comparison. As in the analysis of LWH, the horizontal average is made over the grid points with intense radar echoes and strong wind gusts where the radar reflectivity is larger than 30 dBZ and the wind speed is above the top 30% within the square at each vertical level. It can be seen clearly that as time progresses, the wind speed does increase at almost all altitudes. At 0900 UTC, the maximum wind speed reaching at 40 m/s occurs at $z \sim 1.5$ km; at 1200 UTC, the maximum wind speed is peaked at 47 m/s. This wind profile obviously displays strong horizontal winds of TC Fanapi on the western side of CMR building up from lower levels with time, an indication of bottom-up reformation of TC eyewall structure. Note that another reflectivity threshold of 40 dBZ is also used and the result is generally similar to that shown in Figure 8.

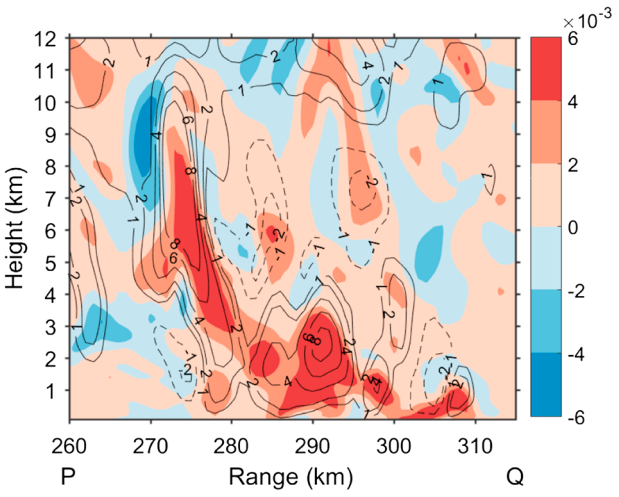

Figure 11. Vertical velocity (contoured; in units of m/s) and vertical vorticity (colored; in units of 10^{-3}/s) of the CTL run at 1030 UTC 19 September 2010 along the vertical cross section PQ marked by the solid line in Figures 9c and 9d.

As indicated by LWH, most of previous observational studies of VHTs used the airborne or spaceborne instruments to discuss the tropical cyclogenesis, while TCs are still over oceans. Similarly, most modeling studies were conducting numerical simulations of VHTs to discuss the oceanic tropical cyclogenesis. To our knowledge, this research and the previous study of LWH are relatively few studies to examine the role of VHTs in TC evolution under the influence of terrain.

Figure 9 shows the evolution of simulated vertical velocity and vertical vorticity at 2-km height of the CTL run during the period of 0900–1100 UTC. The distribution of positive (cyclonic) vorticity (Figures 9b, 9d, and 9f) generally follows the curved rainband and is significantly correlated with the updrafts (Figures 9a, 9c, and 9e). In our study, a VHT is defined as the coexistence of vertically averaged updraft (>0.5 m/s) and positive (cyclonic) vorticity within a vertical column (0.5–10 km), same as the definition used in LWH and generally consistent with those used in Reasor et al. (2005) and

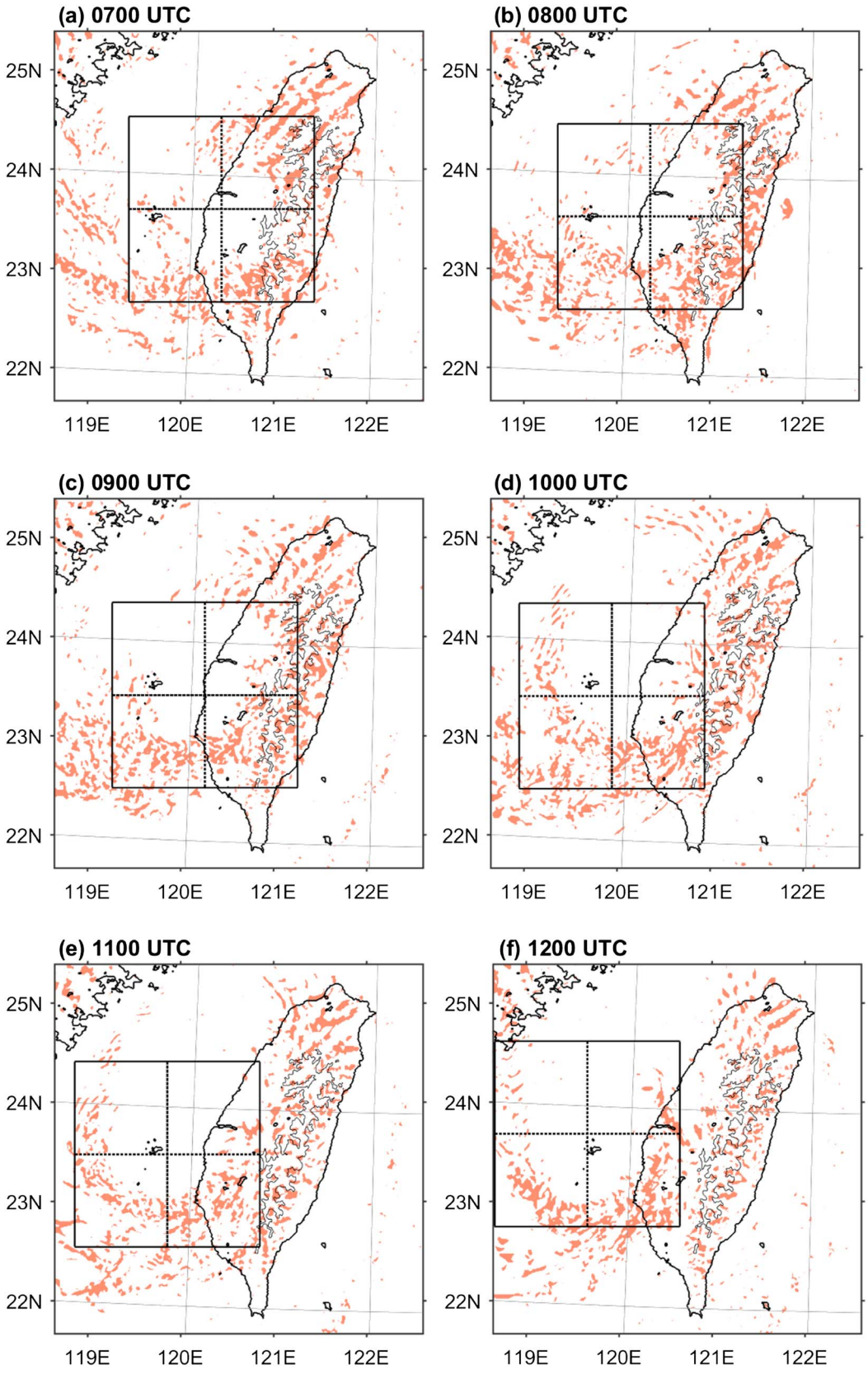

Figure 12. Horizontal distribution of the vortical hot towers shown by the color shading at (a) 0700, (b) 0800, (c) 0900, (d) 1000, (e) 1100, and (f) 1200 UTC 19 September 2010.

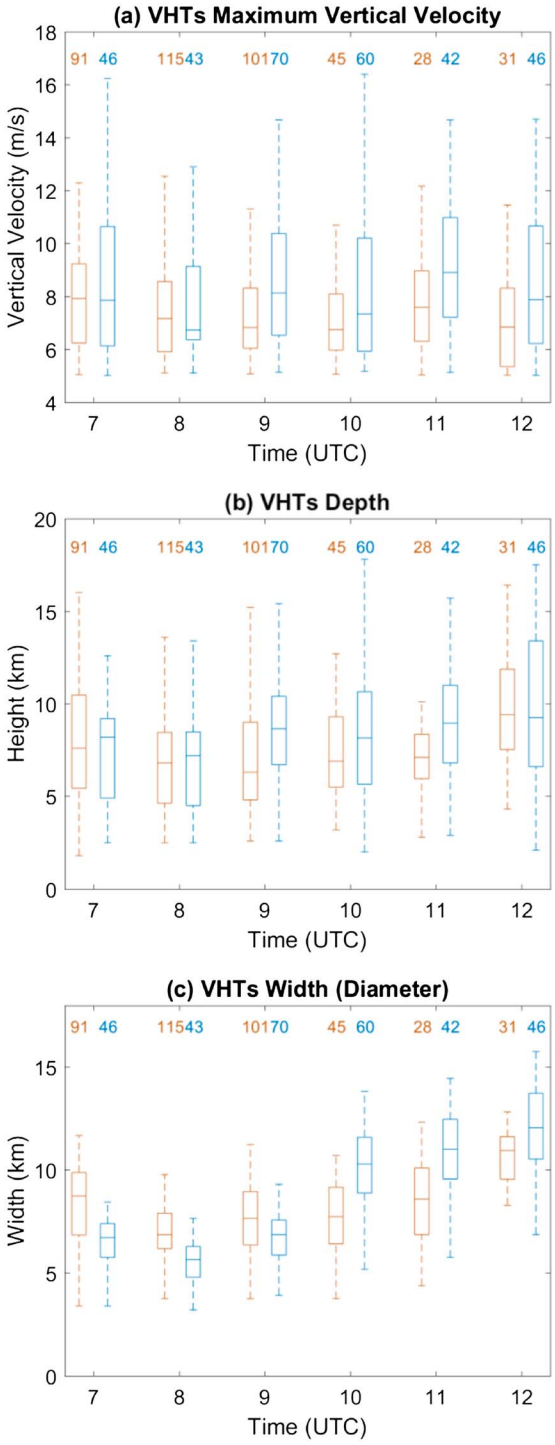

Figure 13. Box-and-whisker plot of maximum vertical velocity (in m/s), depth (in km), and width (in km) of vortical hot towers (VHTs) over land (in red) and ocean (in blue) within a box of 200 km by 200 km centered at the tropical cyclone eye during the time period between 0700 and 1200 UTC 19 September 2010. The red number is the number of VHTs over land, and the blue number is the number of VHTs over ocean. The box-and-whisker plot is interpreted as follows: The middle line shows the median value, the top and bottom of the box show the upper and lower quartiles (i.e., 75th and 25th percentile values), and the whiskers show the minimum and maximum values.

Montgomery et al. (2006). The three-dimensional spatial correlation coefficient between the vertical velocity and vertical vorticity (calculated using Eq. (22) of Tai et al., 2017) within the VHTs inside four squares in Figure 9 is shown in Figure 10. The good spatial correlation between updrafts and cyclonic vorticities, as indicated by the fact that the spatial correlation coefficients between two variables are near 0.5 or above during 0900–1100 UTC, supports the existence of VHTs within the rainband of TC Fanapi.

Figure 11 displays the vertical structure of a simulated VHT over the Taiwan Island. In LWH (see their Figure 16), the VHTs inferred from the observational analysis have relatively weaker updrafts (3–4 m/s), smaller width (~5 km), and shallower depth (~10 km), compared with the stronger (10–20 m/s), wider (~10 km), and deeper (~17 km) VHTs over the ocean documented by Houze Jr. et al. (2009, see their Figures 8 and 14). Our simulated inland VHTs have maximum updrafts of 6–8 m/s, a horizontal width of 5–10 km, and a vertical depth of ~10 km, similar to those characteristics of the inland VHT found in LWH. Hence, terrain and surface friction over land do tend to weaken the updraft intensity and reduce the width and depth of VHTs.

Figure 12 shows the horizontal distribution of VHTs at 2-km height of the CTL run during the time period of 0700–1200 UTC. More organized VHTs occur within the TC rainband at later time (1000–1200 UTC; see Figures 12d–12f), which facilitate upward transport of cyclonic vorticity from low levels to the reformation of the TC eyewall (to be discussed later).

To systematically compare the difference of spatial characteristics between oceanic VHTs and inland VHTs in the CTL run, Figure 13 displays the corresponding statistical distributions of maximum vertical velocity, depth, and width (or diameter) within the box of 200 km by 200 km during the time period of 0700–1200 UTC. The depth of a VHT is defined as the vertical depth between the top and the bottom of a VHT. The bottom of a VHT is the lowest vertical level of an updraft (with positive vertical velocity), and the top of a VHT is the highest vertical level of an updraft (with its vertical velocity of $>$0.5 m/s). The width of a VHT is defined as the area-equivalent diameter of a close region of positive (cyclonic) vorticity with one or several local vorticity maxima. After 0900 UTC when the TC center is near or off the Taiwan coast, the inland VHTs have weaker maximum vertical velocities (with the median value of 7.0–8.0 m/s), shallower depth (with the median value of 6.5–9.0 km), and narrower diameter (with the median value of 7.0–11.5 km); in contrast, the oceanic VHTs have stronger maximum vertical velocities (7.5–9.0 m/s), deeper depth (7.5–9.0 km), and wider diameter (10.0–12.0 km; all in the median value). This statistical difference between oceanic and inland VHTs is consistent with results shown in the cross section in Figure 11. Note that the translation of the analysis box away from the CMR after 0900 UTC might affect the overland distribution of vertical velocities of VHTs inside the analysis area, resulting in less inland VHTs and more oceanic VHTs. This might affect the VHT statistical analysis.

Figure 14 shows the vertical profiles of vertical vorticity horizontally averaged within a box of 200 km by 200 km (enclosing the TC vortex circulation and centered on the TC eye) and temporally averaged during three time periods of 0930–1030, 1030–1130, and 1130–1200 UTC. It illustrates that the magnitude of positive (cyclonic) vorticity is increasing with time,

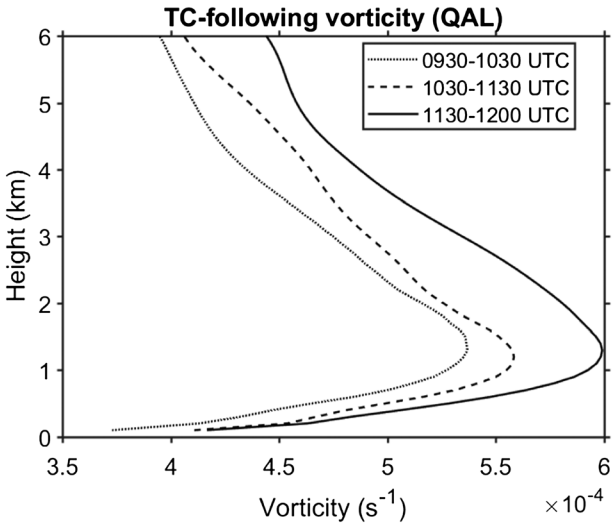

Figure 14. Vertical profiles of vertical vorticity horizontally averaged within a box (200 km by 200 km) with the tropical cyclone (TC) eye located at the box center and temporally averaged during the time periods of 0930–1030, 1030–1130, and 1130–1200 UTC.

particularly at the lower to middle levels (2–6 km), a clear indication of the growth of TC vortex circulation during this time period, although it is not reflected in the time series of storm intensity (Figure 3).

4. Vorticity Budget Analysis

To determine whether the top-down or bottom-up mechanisms are responsible for Fanapi's eyewall reformation, the budget of relative vertical vorticity is calculated. Following the TC motion, the relative vorticity equation in height coordinate can be written as

$$\frac{\partial \zeta}{\partial t} = -\left(\vec{V}_h - \vec{C}\right)\cdot\nabla\zeta - w\frac{\partial \zeta}{\partial z} - \eta\nabla\cdot\vec{V}_h - \hat{k}\cdot\nabla_h w\times\frac{\partial \vec{V}_h}{\partial z} + \hat{k}\cdot(\nabla p\times\nabla\alpha) + R, \quad (1)$$

or

$$\mathrm{TEN} = \mathrm{HAD} + \mathrm{VAD} + \mathrm{STR} + \mathrm{TIL} + \mathrm{SOL} + \mathrm{RSL}, \quad (2)$$

where ζ is relative vorticity, $\vec{C}$ is the translation speed of TC, $\vec{V}_h$ is horizontal wind, and α is specific volume. The term on the left-hand side in equation (1) is the relative vorticity tendency (TEN). Terms on the right-hand side in equation (1) are storm-relative horizontal vorticity advection (HAD), vertical advection (VAD), stretching (STR), tilting (TIL), solenoid (SOL), and residual term (RSL). All the budget terms are calculated in a storm-centric quasi-Lagrangian framework, which is updated every 10 min, following previous studies (Chen & Bosart, 1979; Fang & Zhang, 2010; Huang et al., 2014; Nguyen & Molinari, 2015).

The model outputs are interpolated from the Weather Research and Forecasting (WRF) terrain-following coordinate into the constant-height coordinate. The TC center is defined as TC circulation center at 4-km height, which is above the highest peak of CMR. The vorticity budget calculation starts from 0600 UTC to 1200 UTC 19 September 2010 and lasts for 6 hr.

Since the reformation of Fanapi eyewall starts from 1000 UTC and the VHTs and their collective forcing may have been hypothesized to play an important role in the reformation of the Fanapi eyewall, a vorticity budget diagnosis averaged over the VHTs at this time is conducted. Figure 15 shows the vertical profiles of the vorticity budget terms temporally averaged from 0930 to 1030 UTC and horizontally averaged within the areas

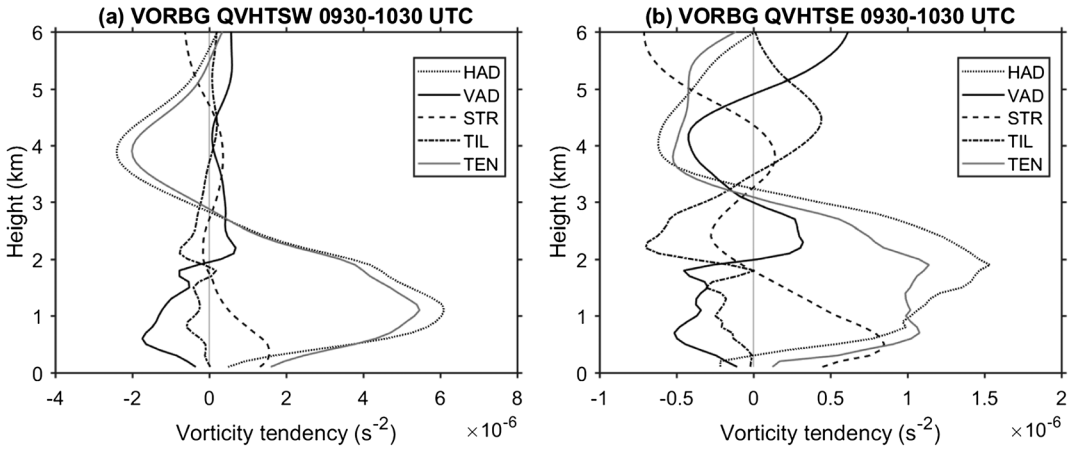

Figure 15. The vertical profiles of the vertical vorticity budget terms averaged within the vortical hot towers in the (a) SW and (b) SE squares to the Fanapi center at 1000 UTC. Results are averaged horizontally within the vortical hot towers inside the square of 100 km by 100 km and temporally from 0930 to 1030 UTC. Horizontal locations of two squares are shown in Figure 12d.

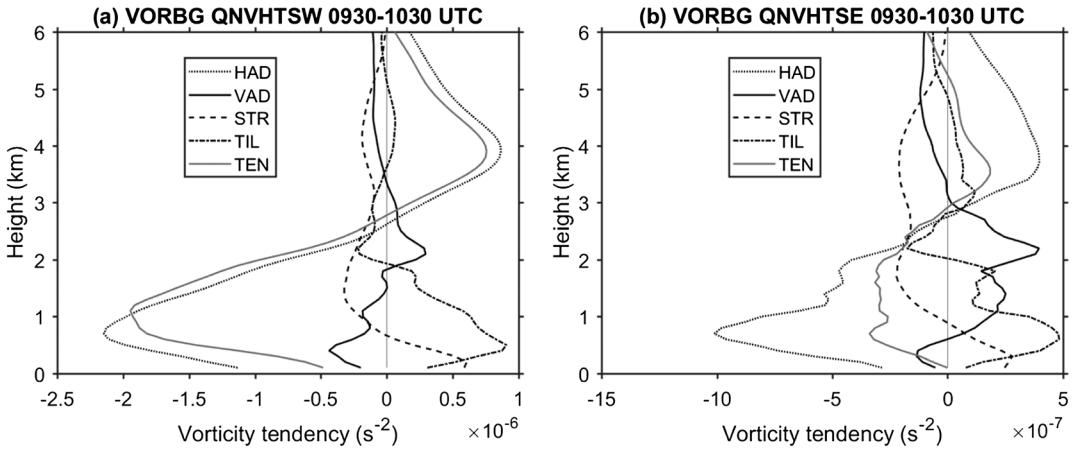

Figure 16. As in Figure 15 except for the non–vortical hot tower (VHT) areas.

encompassed by VHTs in the SW and SE squares (see Figure 12d). Vorticity budget terms averaged over the SW square (Figure 15a) are generally larger than those averaged over the SE square (Figure 15b), mainly because of enhanced surface friction and terrain effects within the SE square.

At lower levels ($z < 3$ km), the HAD plays a leading role in increasing positive vorticity with higher values at the VHTs over the SW square. This is similar to the positive total horizontal vorticity flux at lower levels over the areas with vortex mergers, which aggregately increase the tangential momentum on the TC vortex scale in an axisymmetric framework (Hendricks et al., 2004; see their Eq. (7) and Figure. 8). The STR mechanism produces positive (cyclonic) vorticity TEN at lower levels ($z < 2$ km) and negative (anticyclonic) vorticity TEN at middle levels. VAD reverses sign several times in the vertical on the SE square, possibly by the turbulent updrafts and downdrafts above terrain. TIL term is smaller than other terms and has a weakly negative (anticyclonic) vorticity TEN at low levels (below 2 km) on the SE square. The SOL and RSL terms are much smaller than others (HAD, VAD, STR, and TIL); thus, their profiles are not shown. The net vorticity TEN within the VHTs generates positive vorticity at lower levels ($z < 3$ km) and negative vorticity at middle levels (3 km $< z <$ 6 km) on both squares, resulted predominantly by the HAD. Note that TEN term is directly calculated from model outputs.

The vertical profiles of the vorticity budget terms temporally averaged from 0930 to 1030 UTC and horizontally averaged within the non-VHT regions in the SW and SE squares are shown in Figure 16. Due to larger areas and weaker convection to generate vorticity over the non-VHT regions (i.e., within rainband and eye), the magnitude of the vorticity-budget terms averaged over the non-VHT regions is smaller than their

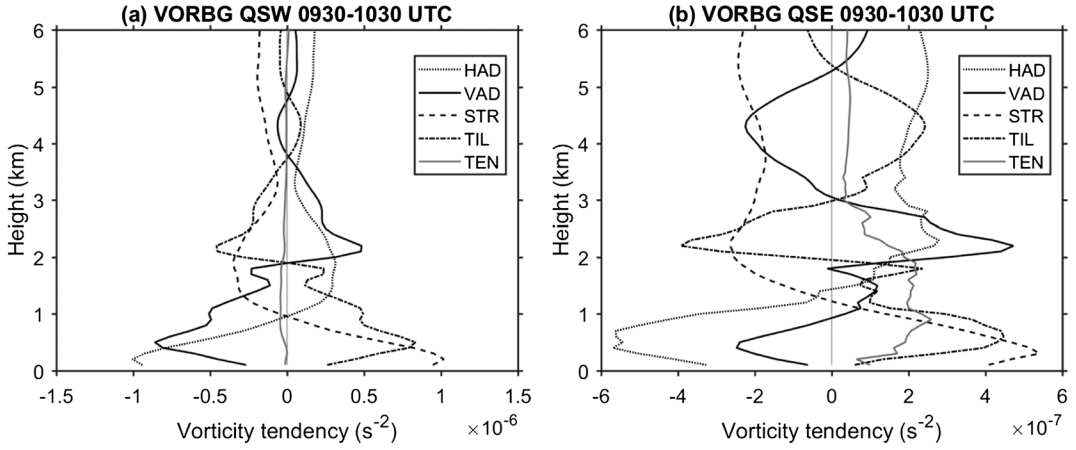

Figure 17. As in Figure 15 except for the whole (a) SW and (b) SE square areas (100 km by 100 km).

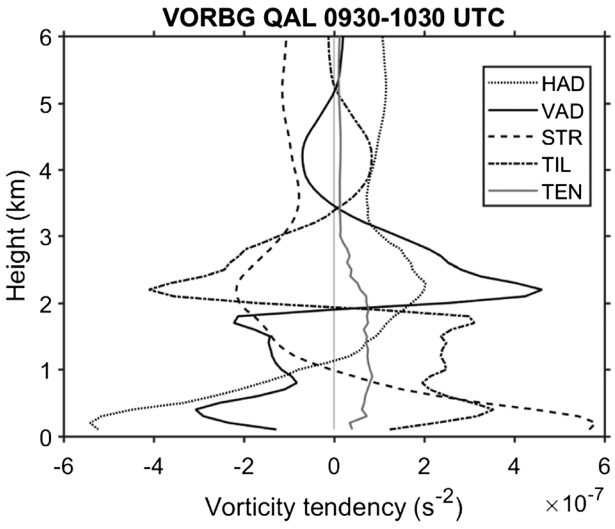

Figure 18. As in Figure 15 except for the box area of 200 km by 200 km with the tropical cyclone eye located at the box center.

counterparts in Figure 15. Similar to those averaged within the VHTs, the STR mechanism produces positive (cyclonic) vorticity TEN at low levels ($z < 1$ km) and negative (anticyclonic) vorticity TEN above ($z > 1$ km). VAD still transports vorticity upward and results in negative vorticity TEN at low levels and positive vorticity TEN at middle levels. TIL generates positive (cyclonic) vorticity TEN at low levels ($z < 2$ km) and negative (anticyclonic) vorticity TEN at middle levels. Note that the HAD generates negative vorticity TEN at low levels and positive vorticity TEN at middle levels, in contrast to those HAD terms averaged within the VHTs (Figure 15). This indicates that at low levels, the HAD process transports positive (cyclonic) vorticity into the VHTs associated with deep convective cores, resulting in negative (anticyclonic) vorticity TEN in the remaining regions with moderate and weak convection. This is in agreement with Houze Jr. et al. (2009), who reported different vorticity characteristics for the convective-scale VHTs (deep vertical column of cyclonic vorticities) and stratiform region (with cyclonic vorticity at mid-to-upper levels) within the analyzed rainband of Hurricane Ophelia (2005; see their Figure 20). The net vorticity TEN over the non-VHT regions generates negative vorticity at lower levels ($z < 2.5$–3 km) and positive vorticity at middle levels (3 km $< z < 6$ km) on both squares, strongly in phase with the HAD term.

Figure 17 displays the vertical profiles of vorticity budget terms horizontally averaged within the whole SW and SE squares and temporally centered at 1000 UTC (averaged in 1-hr period). The vorticity TEN is very small over the SW square (Figure 17a), indicating that the vertical vorticity remains approximately steady during the time period of 0930–1030 UTC. Inside the SE square over land, the vorticity TEN remains positive at lower to middle levels ($z < 6$ km), which is mainly associated with the HAD within the VHTs (HAD profile in Figure 15b). The positive vorticity TEN at low-to-middle levels (Figure 17b) is in agreement with more cyclonic vorticity patches shown inside the SE square (see Figure 9d).

Figure 18 shows the vertical profiles of the vorticity budget terms horizontally averaged within the entire TC vortex circulation (inside a box of 200 km by 200 km centered at the TC eye) and temporally averaged from 0930 to 1030 UTC. Note that the vertical profiles for vertical vorticity budget terms averaged for the entire TC vortex circulation are similar to those averaged over the SE square (particularly for the TEN term; Figure 17b), indicating the dominant influence by the SE square with lots of organized VHTs over the terrain. The positive (cyclonic) vorticity TEN for the TC vortex circulation is consistent with the increase of cyclonic vorticity from lower to middle levels shown in Figure 14, supporting the bottom-up reformation of TC vortex circulation and eyewall structure after 1000 UTC.

5. The No-Terrain and No-Latent-Heating Experiments

The existence of the CMR on Taiwan imposes a strong effect on the track of Fanapi and the asymmetric structure of precipitation. For the NTR experiment with no topography on Taiwan (but still with a flat land), the simulated Fanapi has a straight westward track, instead of a track deviated to the south as a result of terrain blocking and channel effects (Figure 2). The VHTs in NTR experiment are highly organized and confined within the eyewall (Figure 19), compared with the asymmetric distribution of VHTs in the CTL run (Figure 12). The radar reflectivity field in the NTR experiment is highly symmetric (Figure 20), instead of an asymmetric structure in the precipitation field (Figures 4 and 5). The weaker and less VHTs in central Taiwan in the CTL experiment (Figures 12a–12c) may be associated with suppression of deep convection by the strong downslope winds on the lee (western) side of the CMR (Figures 6a–6c) at 0700–0900 UTC. However, the VHTs in the CTL storm over the Taiwan Strait remain organized along the rainband (see the VHTs in the SW squares; Figures 12d and 12e) and are propagated toward the SE squares (next to the western edge of the CMR) by the tangential flow. These organized VHTs in the SE squares (Figure 12f) help transport cyclonic vorticity into middle levels and then cooperate with the rich vorticity within the rainband to rebuild the Fanapi eyewall.

In the NLH experiment where the latent heating and cooling is turned off 3 hr before Fanapi made landfall on Taiwan Island (i.e., no latent heating and cooling after 0000 UTC 19 September), the simulated storm is

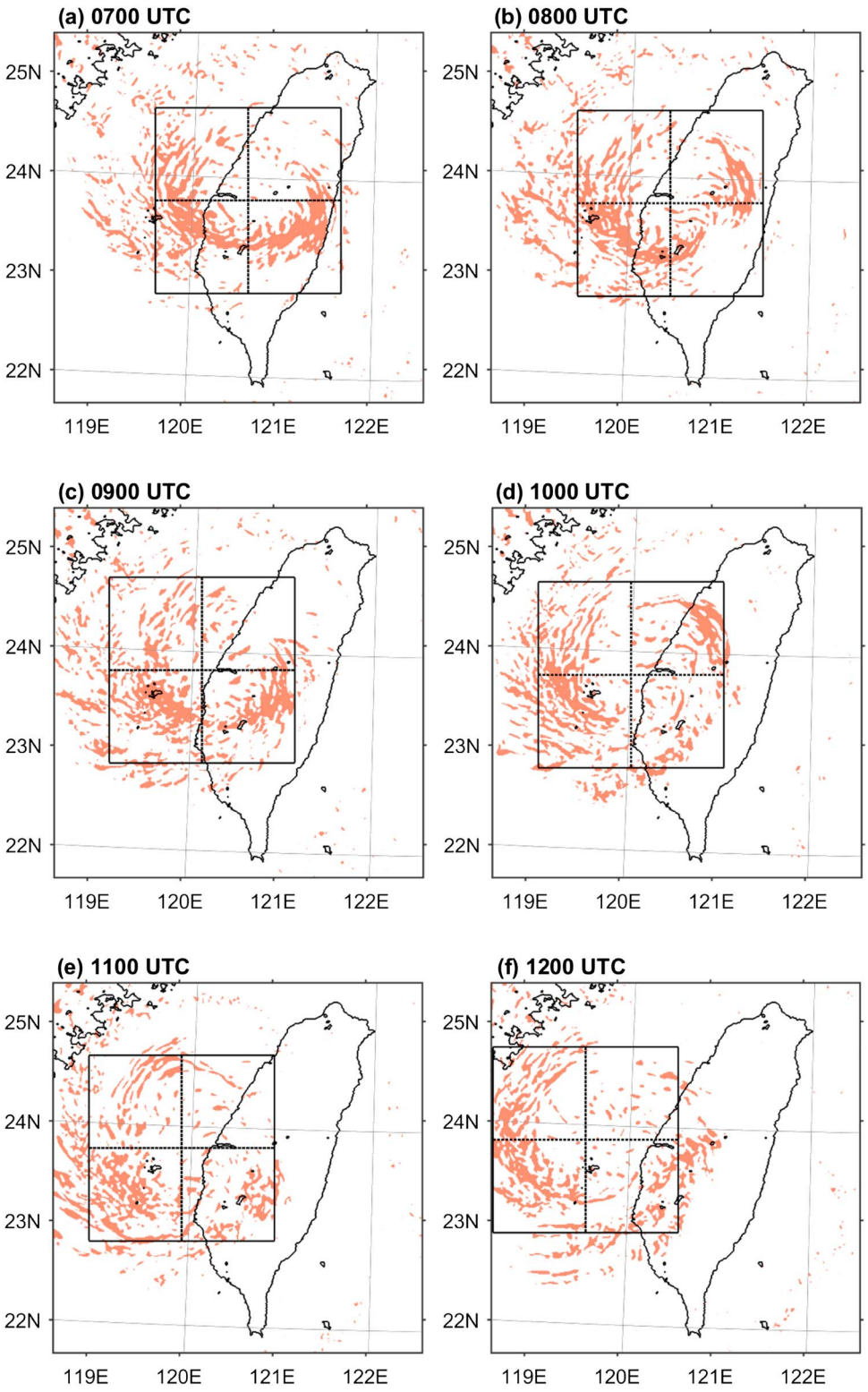

Figure 19. As in Figure 12 except for the no-terrain experiment.

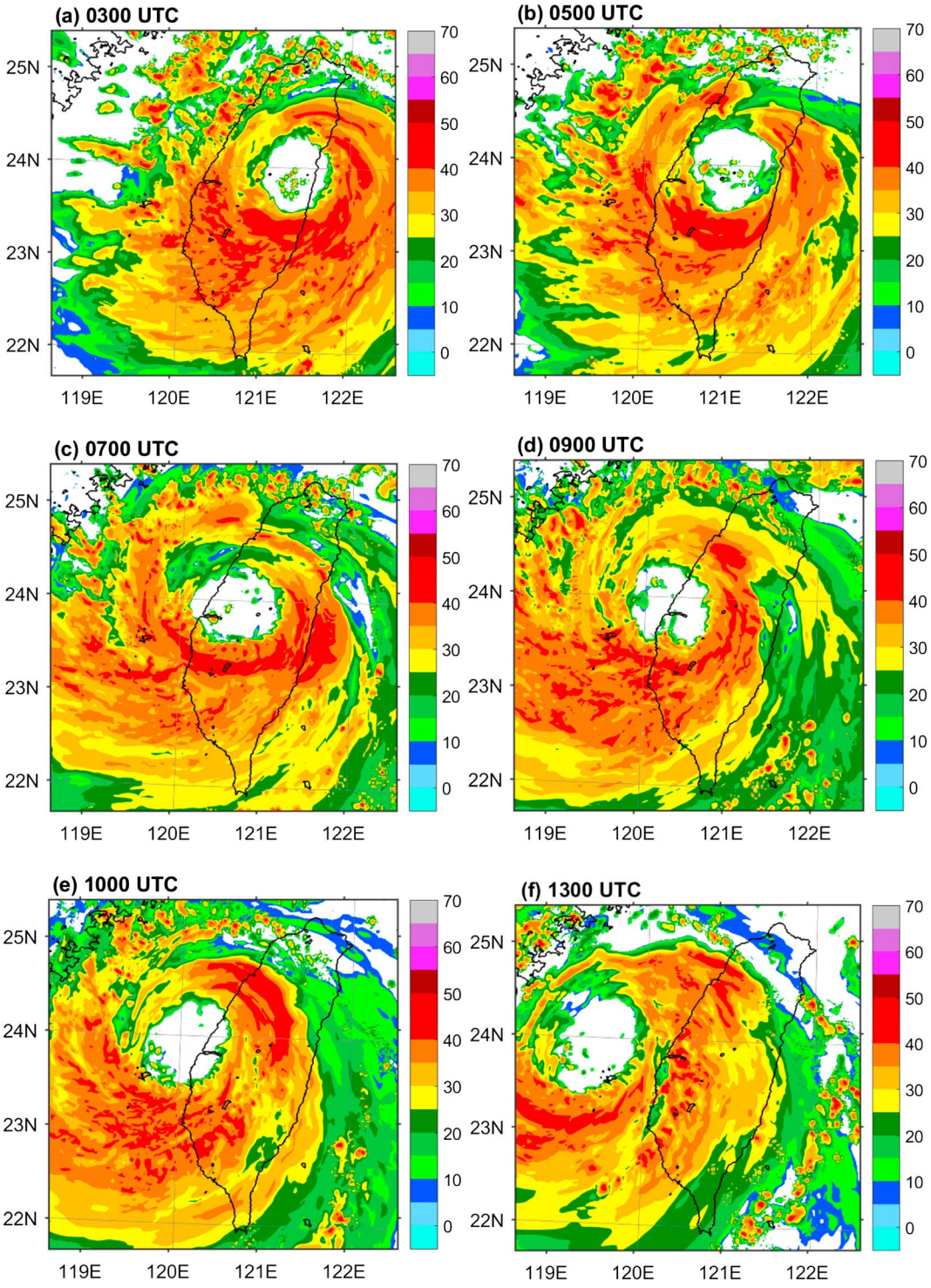

Figure 20. As in Figure 5 except for the no-terrain experiment.

quickly weakened and dissipated. Figure 21 displays the horizontal distribution of VHTs of the NLH experiment at 0700 UTC 19 September. It is shown that in the absence of latent heat release, the VHTs quickly decay and radiate outward from the eyewall as gravity-wave perturbations. This clearly illustrates the importance of latent heating/cooling process in the generation of VHTs and the maintenance of Fanapi vortex circulation.

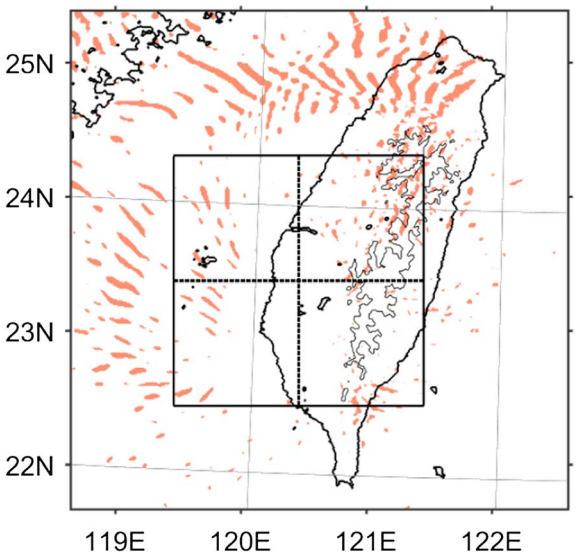

Figure 21. As in Figure 12 except for the no-latent-heating experiment at 0700 UTC.

6. Conclusions

Typhoon Fanapi made landfall on eastern Taiwan at 0000 UTC 19 September and left Taiwan at 1200 UTC 19 September 2010, producing heavy rainfall and severe floods over southwestern Taiwan. When Fanapi approached eastern Taiwan from the ocean, the eyewall gradually weakened and broke down over steep terrains of the CMR. Typhoon Fanapi continued its westward track with a southward deflection and a significant tilt of the circulation center while crossing the CMR. If there was no terrain on Taiwan Island, Fanapi would continue its westward movement without any deflection, the eyewall remained intact, and had no vertical tilt of the circulation center. The observational study of LWH documented Fanapi's eyewall reformation on Taiwan Island with multiple-Doppler radar analyses and surface station data and indicated a possible bottom-up process for the eyewall reconstruction over the southwestern plain of the CMR. Through numerical sensitivity experiments and detailed vorticity-budget analysis, this study further confirms that the bottom-up process was indeed active to reorganize the eyewall of Typhoon Fanapi (2010) over land.

This study and the observation study of LWH are among few studies that have investigated the role of VHTs in TC eyewall reformation under the influence of terrain. A statistical comparison of the median value indicates that the VHTs over land have weaker maximum updrafts (7.0–8.0 m/s), narrower diameter (7.5–11.5 km), and shallower depth (6.5–9.0 km), compared with the stronger maximum updrafts (7.5–9.0 m/s), wider (10.0–12.0 km), and deeper (7.5–9.0 km) VHTs over the Taiwan Strait. Topography and surface friction over land may weaken the updraft intensity and reduce the width and depth of VHTs. Also, the thermodynamic factor that there are less moisture and heat fluxes over land than those over ocean may also contribute to these inland VHTs with weaker maximum updrafts, narrower diameters, and shallower depths.

At low levels ($z < 3$ km), the HAD process transports positive (cyclonic) vorticity into the VHTs in association with deep convective cores, resulting in negative (anticyclonic) vorticity TEN in the remaining regions with moderate and weak convection. Similarly, Houze Jr. et al. (2009) also found different vorticity characteristics for the convective-scale VHTs and stratifrom region. The net vorticity tendencies averaged within the VHTs and non-VHT regions are under strong influence of HAD.

The existence of the CMR terrain on Taiwan imposes asymmetric distribution of VHTs along the rainbands and eyewall of TC Fanapi. The suppression of deep convection by the strong downslope winds on the lee (western) side of the CMR weakens the VHTs in central Taiwan. In contrast, the VHTs over the Taiwan Strait remain organized (and maintained by latent heat release) along the rainband and are propagated toward the southeast quadrant over land by the TC tangential flow. These organized VHTs in the southeast quadrant of TC Fanapi help transport cyclonic vorticity into middle levels and then cooperate with the rich vorticity within the rainband by HAD to rebuild the Fanapi eyewall. Without the latent heat release, the VHTs quickly decay and radiate outward from the eyewall as gravity-wave perturbations.

The vorticity balance within the entire TC vortex circulation at 1000 UTC is largely dominated by its southeast quadrant with lots of organized VHTs over the Taiwan terrain. The net positive vorticity TEN for the TC circulation at low-to-middle levels at 1000 UTC is consistent with the increase of cyclonic vorticity from lower to middle levels, supporting the bottom-up reformation of TC vortex circulation and eyewall structure after 1000 UTC.

Although the control simulation bears close resemblance with the observational analyses, we should keep in mind that the conclusions reached from this modeling study are mainly based on numerical simulations with typhoon track and intensity errors, model deficiencies, and physics uncertainties. Typhoon Fanapi (2010) is a rare TC case with observational data from multiple Doppler radars to document its reformation process over land. More case studies are required to generalize the findings from this particular typhoon case to other TCs in other geographical locations (such as the Atlantic Ocean, Indian Ocean, or Australia).

Acknowledgments
We appreciate three anonymous reviewers' helpful comments, which significantly improve the quality of this manuscript. This work was supported by the Ministry of Science and Technology of Taiwan under grants MOST 105-2119-M-002-026 and MOST 105-2625-M-002-021 and the Central Weather Bureau under grant MOTC-CWB-105-M-07. The observation data are available from the Typhoon Databank of Central Weather Bureau (http://rdc8.cwb.gov.tw). The ECMWF/TOGA data are available from Research Data Archive (https://rda.ucar.edu/datasets/ds111.1/). The model simulations were performed and archived at National Taiwan University (http://rain.as.ntu.edu.tw/Fanapi.htm).

References

Chang, S. W. (1982). The orographic effects induced by an island mountain range on propagating tropical cyclones. *Monthly Weather Review*, *110*(9), 1255–1270. https://doi.org/10.1175/1520-0493(1982)110<1255:TOEIBA>2.0.CO;2

Chen, T. J. G., & Bosart, L. F. (1979). A quasi-Lagrangian vorticity budget of composite cyclone-anticyclone couplets accompanying North American polar air outbreaks. *Journal of the Atmospheric Sciences*, *36*(2), 185–194. https://doi.org/10.1175/1520-0469(1979)036<0185:AQLVBO>2.0.CO;2

Chou, K.-H., Wu, C.-C., & Wang, Y. (2011). Eyewall evolution of typhoons crossing the Philippines and Taiwan: An observational study. *Terrestrial, Atmospheric and Oceanic Sciences*, *22*(6), 535–548. https://doi.org/10.3319/TAO.2011.05.10.01(TM)

Dudhia, J. (1989). Numerical study of convection observed during the winter monsoon experiment using a mesoscale two-dimensional model. *Journal of the Atmospheric Sciences*, *46*(20), 3077–3107. https://doi.org/10.1175/1520-0469(1989)046<3077:NSOCOD>2.0.CO;2

Fang, J., & Zhang, F. (2010). Initial development and genesis of Hurricane Dolly (2008). *Journal of the Atmospheric Sciences*, *67*(3), 655–672. https://doi.org/10.1175/2009JAS3115.1

Grell, G. A., & Dévényi, D. (2002). A generalized approach to parameterizing convection combining ensemble and data assimilation techniques. *Geophysical Research Letters*, *29*(14), 1693. https://doi.org/10.1029/2002GL015311

Hendricks, E. A., Montgomery, M. T., & Davis, C. A. (2004). The role of "vortical" hot towers in the formation of Tropical Cyclone Diana (1984). *Journal of Atmospheric and Solar*, *61*(11), 1209–1232. https://doi.org/10.1175/1520-0469(2004)061<1209:TROVHT>2.0.CO;2

Hong, S.-Y., & Pan, H.-L. (1996). Nonlocal boundary layer vertical diffusion in a medium-range forecast model. *Monthly Weather Review*, *124*(10), 2322–2339. https://doi.org/10.1175/1520-0493(1996)124<2322:NBLVDI>2.0.CO;2

Houze, R. A. Jr., Lee, W.-C., & Bell, M. M. (2009). Convective contribution to the genesis of Hurricane Ophelia (2005). *Monthly Weather Review*, *137*(9), 2778–2800. https://doi.org/10.1175/2009MWR2727.1

Huang, C.-Y., Wu, I.-H., & Feng, L. (2016). A numerical investigation of the convective systems in the vicinity of southern Taiwan associated with Typhoon Fanapi (2010): Formation mechanism of double rainfall peaks. *Journal of Geophysical Research, [Atmospheres]*, *121*, 12,647–12,676. https://doi.org/10.1002/2016JD025889

Huang, H.-L., Yang, M.-J., & Sui, C.-H. (2014). Water budget and precipitation efficiency of Typhoon Morakot (2009). *Journal of the Atmospheric Sciences*, *71*(1), 112–129. https://doi.org/10.1175/JAS-D-13-053.1

Huang, Y.-H., Wu, C.-C., & Wang, Y. (2011). The influence of island topography on typhoon track deflection. *Monthly Weather Review*, *139*(6), 1708–1727. https://doi.org/10.1175/2011MWR3560.1

Jian, G.-J., & Wu, C.-C. (2008). A numerical study of the track deflection of Supertyphoon Haitang (2005) prior to its landfall in Taiwan. *Monthly Weather Review*, *136*(2), 598–615. https://doi.org/10.1175/2007MWR2134.1

Knievel, J. C., Bryan, G. H., & Hacker, J. P. (2007). Explicit numerical diffusion in the WRF model. *Monthly Weather Review*, *135*(11), 3808–3824. https://doi.org/10.1175/2007MWR2100.1

Lee, C.-S., Liu, Y.-C., & Chien, F.-C. (2008). The secondary low and heavy rainfall associated with Typhoon Mindulle (2004). *Monthly Weather Review*, *136*(4), 1260–1283. https://doi.org/10.1175/2007MWR2069.1

Lin, Y.-L., Chen, S.-Y., Hill, C. M., & Huang, C.-Y. (2005). Control parameters for the influence of a mesoscale mountain range on cyclone track continuity and deflection. *Journal of the Atmospheric Sciences*, *62*(6), 1849–1866. https://doi.org/10.1175/JAS3439.1

Lin, Y.-L., Ensley, D. B., Chiao, S., & Huang, C.-Y. (2002). Orographic influences on rainfall and track deflection associated with the passage of a tropical cyclone. *Monthly Weather Review*, *130*(12), 2929–2950. https://doi.org/10.1175/1520-0493(2002)130<2929:OIORAT>2.0.CO;2

Lin, Y.-L., Han, J., Hamilton, D. W., & Huang, C.-Y. (1999). Orographic influence on drifting cyclones. *Journal of Atmospheric and Solar*, *56*(4), 534–562. https://doi.org/10.1175/1520-0469(1999)056<0534:OIOADC>2.0.CO;2

Liou, Y.-C., Wang, T.-C. C., & Huang, P.-Y. (2016). The inland eyewall reintensification of Typhoon Fanapi (2010) documented from an observational perspective using multiple-Doppler radar and surface measurements. *Monthly Weather Review*, *144*(1), 241–261. https://doi.org/10.1175/MWR-D-15-0136.1

Mlawer, E. J., Taubman, S. J., Brown, P. D., Iocono, M. J., & Clough, S. A. (1997). Radiative transfer for inhomogeneous atmospheres: RRTM, a validated correlated-k model for the longwave. *Journal of Geophysical Research*, *102*(D14), 16,663–16,682. https://doi.org/10.1029/97JD00237

Montgomery, M. T., Nicholls, M. E., Cram, T. A., & Saunders, A. B. (2006). A vortical hot tower route to tropical cyclogenesis. *Journal of the Atmospheric Sciences*, *63*(1), 355–386. https://doi.org/10.1175/JAS3604.1

Morrisson, H., Curry, J. A., & Khvorostyanov, V. I. (2005). A new double-moment microphysics parameterization for application in cloud and climate models. Part I: Description. *Journal of the Atmospheric Sciences*, *62*(6), 1665–1677. https://doi.org/10.1175/JAS3446.1

Morrisson, H., & Gettelman, A. (2008). A new two-moment bulk stratiform cloud microphysics scheme in the Community Atmosphere Model, Version 3 (CAM3). Part I: Description and numerical tests. *Journal of Climate*, *21*(15), 3642–3659. https://doi.org/10.1175/2008JCLI2105.1

Nguyen, L. T., & Molinari, J. (2015). Simulation of the downshear reformation of a tropical cyclone. *Journal of the Atmospheric Sciences*, *72*(12), 4529–4551. https://doi.org/10.1175/JAS-D-15-0036.1

Reasor, P. D., Montgomery, M. T., & Bosart, L. F. (2005). Mesoscale observations of the genesis of Hurricane Dolly (1996). *Journal of the Atmospheric Sciences*, *62*(9), 3151–3171. https://doi.org/10.1175/JAS3540.1

Sippel, J. A., Nielsen-Grammon, J. W., & Allen, S. E. (2006). The multiple vortex nature of tropical cyclogenesis. *Monthly Weather Review*, *134*(7), 1796–1814. https://doi.org/10.1175/MWR3165.1

Skamarock, W. C., Klemp, J. B., Dudhia, J., Gill, D. O., Barker, D. M., Duda, M. G., et al. (2008). A description of the Advanced Research WRF version 3, NCAR Tech. Note NCAR/TN–475+STR, 113 pp.

Tai, S.-L., Liou, Y.-C., Sun, J., & Chang, S.-F. (2017). The development of a terrain-resolving scheme for the forward model and its adjoint in the four-dimensional variational Doppler radar analysis system (VDRAS). *Monthly Weather Review*, *145*(1), 289–306. https://doi.org/10.1175/MWR-D-16-0092.1

Wu, C.-C., Chen, S.-G., Yang, C.-C., Lin, P.-H., & Aberson, S. D. (2012). Potential vorticity diagnosis of the factors affecting the track of Typhoon Sinlaku (2008) and the impact from dropwindsonde data during T-PARC. *Monthly Weather Review*, *140*(8), 2670–2688. https://doi.org/10.1175/MWR-D-11-00229.1

Wu, C.-C., Cheng, H.-J., Wang, Y., & Chou, K.-H. (2009). A numerical investigation of the eyewall evolution in a landfalling typhoon. *Monthly Weather Review*, *137*(1), 21–40. https://doi.org/10.1175/2008MWR2516.1

Wu, C.-C., Chou, K.-H., Cheng, H.-J., & Wang, Y. (2003). Eyewall contraction, breakdown and reformation in a landfalling typhoon. *Geophysical Research Letters*, *30*(17), 1887. https://doi.org/10.1029/2003GL017653

Wu, C.-C., & Kuo, Y.-H. (1999). Typhoons affecting Taiwan: Current understanding and future challenges. *Bulletin of the American Meteorological Society*, *80*(1), 67–80. https://doi.org/10.1175/1520-0477(1999)080<0067:TATCUA>2.0.CO;2

Wu, C.-C., Yen, T.-H., Kuo, Y.-H., & Wang, W. (2002). Rainfall simulation associated with Typhoon Herb (1996) near Taiwan. Part I: The topographic effect. *Weather and Forecasting*, *17*(5), 1001–1015. https://doi.org/10.1175/1520-0434(2003)017<1001:RSAWTH>2.0.CO;2

Xue, M. (2000). High-order monotonic numerical diffusion and smoothing. *Monthly Weather Review*, *128*(8), 2853–2864. https://doi.org/10.1175/1520-0493(2000)128<2853:HOMNDA>2.0.CO;2

Yang, M.-J., Zhang, D.-L., & Huang, H.-L. (2008). A modeling study of Typhoon Nari (2001) at landfall. Part I: Topographic effects. *Journal of the Atmospheric Sciences*, *65*(10), 3095–3115. https://doi.org/10.1175/2008JAS2453.1

Yeh, T.-C., & Elsberry, R. L. (1993a). Interaction of typhoons with the Taiwan orography. Part I: Upstream track deflections. *Monthly Weather Review*, *121*(12), 3193–3212. https://doi.org/10.1175/1520-0493(1993)121<3193:IOTWTT>2.0.CO;2

Yeh, T.-C., & Elsberry, R. L. (1993b). Interaction of typhoons with the Taiwan orography. Part II: Continuous and discontinuous tracks across the island. *Monthly Weather Review*, *121*(12), 3213–3233. https://doi.org/10.1175/1520-0493(1993)121<3213:IOTWTT>2.0.CO;2